Apparent Diffusion Coefficient fMRI shines a new light on white matter resting-state connectivity, as compared to BOLD

Inès de Riedmatten[1,2*], Arthur P C Spencer[1,2], Wiktor Olszowy[3,4], Ileana O Jelescu[1,2]

[1]Department of Radiology, Lausanne University Hospital (CHUV), Lausanne, Switzerland,

[2]School of Biology and Medicine, University of Lausanne, Lausanne, Switzerland,

[3]Ecole Polytechnique Fédérale de Lausanne (EPFL), Lausanne, Switzerland,

[4]Data Science Unit, Science and Research, dsm-firmenich AG, Kaiseraugst, Switzerland,

*Correspondence: ines.de-riedmatten@chuv.ch

Abstract: Resting-state functional MRI (rs-fMRI) detects spontaneous low-frequency oscillations in the MRI signal at rest. When they occur simultaneously in distant brain regions, they define functional connectivity (FC) between these regions. While blood oxygen level-dependent (BOLD) fMRI serves as the most widely used contrast for rs-fMRI, its reliance on neurovascular coupling poses challenges in accurately reflecting neuronal activity, resulting in limited spatial and temporal specificity and reduced sensitivity in white matter regions. To overcome these limitations, apparent diffusion coefficient fMRI (ADC-fMRI) is emerging as a promising alternative. This approach captures neuronal activity by monitoring changes in ADC resulting from activity-driven neuromorphological alterations such as transient cell swelling. Using graph theory analysis of resting-state FC networks, this study confirms that ADC-fMRI mirrors the positive correlations observed in BOLD-fMRI in the gray-to-gray matter edges (GM-GM), while diverging significantly from BOLD-fMRI for white-to-white matter (WM-WM) connections. While comparable average clustering and average node strength were found for GM-GM connections, higher average clustering ($p < 10^{-3}$) and average node strength ($p < 10^{-3}$) for ADC-fMRI in WM-WM edges suggests that it captures different information to BOLD in the WM. In addition, a significantly higher FC similarity between subjects for ADC-fMRI (mean 0.70, 95% CI [0.68, 0.72]) than BOLD-fMRI (0.38 [0.31, 0.44]) in WM-WM connections suggests a higher reliability of ADC-fMRI in this brain tissue type, demonstrating its broader applicability across the entire brain and reduced sensitivity to

physiological noise. Taken together, these results indicate a higher sensitivity and robustness of ADC-fMRI in the WM, and encourage its use, together with careful mitigation of vascular contributions, to further investigate WM functional connectivity.

Keywords: Apparent diffusion coefficient, ADC-fMRI, diffusion fMRI, resting state, functional connectivity, white matter connectivity

1 Introduction

First introduced in 1995 by Biswal et al. (1995), resting-state functional MRI (rs-fMRI) historically studies the spontaneous low frequency oscillations (< 0.1 Hz) of the Blood Oxygen Level-Dependent (BOLD) signal at rest (Soares et al., 2016; Tjandra et al., 2005). The coherent functional patterns observed consistently across individuals are referred to as the Resting State Networks (RSNs), such as the Default Mode Network (DMN), originally defined by Raichle et al. (2001) using PET. Typically, brain functional connectivity (FC) can be built from temporal statistical dependence between MRI timeseries across different brain regions and summarized as networks (Babaeeghazvini et al., 2021). In this context, an anatomical or functional parcellation forms the nodes of the network, while a measure of FC forms the network edges ("weights" or "connections") (Lv et al., 2018). Subsequently, the properties of FC networks can be evaluated by computing graph theoretical metrics on brain networks. The ability of FC to capture significant changes in normal resting-state brain activity has clinical relevance in the context of disease or disorder (van den Heuvel & Hulshoff Pol, 2010). For instance, one promising application of rs-fMRI is as a potential aid for preoperative surgical planning to localize the eloquent cortex, as proposed by Zhang et al. (2009) for brain tumor resection. Stampacchia et al. (2022) also provided preliminary evidence that resting-state fMRI could be used for clinical fingerprinting, to detect individual FC alterations following cognitive decline.

In most of the applications to date, fMRI relies on BOLD contrast, whose neurovascular coupling poses challenges in accurately reflecting neuronal activity, resulting in limited spatial and temporal specificity in the GM and WM, and reduced sensitivity in the WM. Indeed, the signal detected with BOLD-fMRI originates from neighboring veins, not directly from neural activity, thus its area extends beyond the neighborhood of the active neurons. In addition, BOLD response also has limited temporal specificity, as its onset is delayed relative to the neuronal activity onset. Furthermore, it displays reduced sensitivity in the WM regions, where BOLD low frequency oscillations, blood flow and blood volume are reduced by 60% (Biswal et al., 1995; Zuo et al., 2010), 75% and 75%, respectively (Gore et al., 2019). Historically,

BOLD-fMRI signal in the WM has commonly been regressed out as a nuisance variable, although it is now receiving renewed attention (Gore et al., 2019; Grajauskas et al., 2019). Despite reduced sensitivity, BOLD hemodynamic response functions (HRFs) were derived in the superficial, middle and deep WM (M. Li et al., 2019). While the superficial WM HRF was found to resemble the GM HRF, an increasing time to peak and a decreasing amplitude were reported with increasing depth of the WM tissue. The physiological validity of these WM HRFs remains to be established. Finally, when vasculature is impaired, such as observed in healthy aging (West et al., 2019), brain tumors (Pak et al., 2017) or multiple sclerosis (Christiansen, 2012), the BOLD response can be altered (Abe et al., 2020), even when the neuronal activity is not affected (Mark et al., 2015).

The potential of using the apparent diffusion coefficient (ADC) of water molecules as an alternative rs-fMRI contrast was first investigated in 2020 in mice (Abe et al., 2020) and in 2021 in humans (Olszowy et al., 2021). As highlighted by Darquié et al. (2001), this diffusion-based contrast is sensitive to neuronal activity via neuromorphological or neuromechanical coupling, although the precise mechanism behind ADC-fMRI remains incompletely understood (Abe et al., 2020). Briefly, fluctuations in tissue microstructure resulting from brain activity influence the random Brownian motion of water molecules, and are detected as a transient alteration of the ADC at the voxel-level (Bammer, 2003). A decrease in ADC was thus observed immediately after the application of a stimulus (Nunes et al., 2021; Olszowy et al., 2021), possibly due to neuronal swelling. Indeed, nanometer-scale swelling of neuronal somas (Ling et al., 2020), neurites (Ling et al., 2020), myelinated axons (Kwon et al., 2023), synaptic boutons (Chéreau et al., 2017) and astrocytic processes (Sherpa et al., 2016) were observed during neuronal activity.

Since it was first proposed by Darquié et al. (2001), diffusion fMRI (dfMRI) has faced major criticism, including potential BOLD contamination (Miller et al., 2007) and limited sensitivity (Bai et al., 2016). The non-vascular nature of the diffusion-weighted functional signal has however been extensively documented in the literature. It was shown in living mice that aquaporin-4 blocker (astrocyte function perturbator) notably enhanced the BOLD response induced by optogenetic activation of astrocytes, while showing no impact on the dfMRI signal (Komaki et al., 2020). Similarly, when rats were exposed to the neurovascular coupling inhibitor nitroprusside (causing vasodilation and hypotension), the BOLD signal was notably affected, while the dfMRI signal was not (Tsurugizawa et al., 2013). These findings suggest an underlying mechanism for dfMRI which is independent of neurovascular coupling. Nonetheless, under hypercapnia, which should elicit vasodilation without changes in neural activity, the diffusion-weighted fMRI signal up to b = 2400 s mm^{-2} exhibited BOLD-like fluctuations (Miller et al., 2007). Indeed, the diffusion-weighted signal demonstrates sensitivity to T_2 variations ($S(b,t) = S_0 e^{\frac{-TE}{T_2(t)}} e^{-bADC(t)}$), essentially capturing the fundamental mechanism underlying BOLD signal. ADC-fMRI can be used to

overcome this important limitation by calculating an ADC timeseries from the diffusion-weighted signals. The ADC is calculated from a ratio of two diffusion-weighted signals, where the T_2-weighting is largely cancelled out (Eq. 1).

$$ADC(t) = -\frac{1}{b_2 - b_1} ln \left(\frac{S(b_2, t + \delta t)}{S(b_1, t)} \right) \tag{1}$$

However, T_2-weighting is not the sole vascular contribution to the dfMRI signal that requires mitigation. During the hemodynamic response, magnetic susceptibility-induced background field gradients (G_s) vary around blood vessels (Pampel et al., 2010). These gradients impact the diffusion-weighted signal and the ADC by contributing to the effective b-value (Eq. 2).

$$b = xG_D^2 + yG_D G_s(t) + zG_s^2(t) \tag{2}$$

To counteract this, acquisition schemes which minimize cross-terms between diffusion gradients and background gradients, such as Twice-Refocused Spin-Echo (TRSE), can be used instead of the traditional Pulse-Gradient Spin-Echo (PGSE) sequence (Pampel et al., 2010).

Finally, the selection of the two b-values b_1 and b_2 for ADC calculation is also crucial. In previous studies, b_1 was often set to 0. However, applying a small diffusion weighting instead ($b_1 = 200$ s mm^{-2}) largely suppresses fast moving spins from the blood water pool and is therefore recommended to minimize the sensitivity of ADC functional changes to blood volume changes in the voxel (Le Bihan et al., 2006; Olszowy et al., 2021). Indeed, b $= 200$ s mm^{-2} is close to the cut-off typically used to separate capillary perfusion from diffusion in Intra-Voxel Incoherent Motion techniques, for example (Le Bihan, 2019).

Taken together, these criteria provide an ADC-fMRI acquisition that is closely related to neuronal activity, both spatially and temporally, relying on neuromorphological coupling rather than neurovascular coupling. Furthermore, ADC-fMRI by design should be much less affected by physiological noise. Indeed, cardiac and respiratory fluctuations are expected to be largely canceled out when taking the signal ratio of two consecutive images to calculate an ADC (Eq. 1), and ADC-fMRI thus to generate more reproducible results (Zuo et al., 2010). Finally, ADC-fMRI could be particularly beneficial in the WM, where BOLD-fMRI sensitivity is dramatically reduced (Biswal et al., 1995; Gore et al., 2019). As microstructural changes during neuronal activity also occur at the axonal level (Kwon et al., 2023), the applicability of resting-state ADC-fMRI can be extended to WM activity, as already shown using task-fMRI (Spees et al., 2013).

The aim of this study was to examine the feasibility of utilizing ADC timecourses in resting-state fMRI

and to determine whether it could provide additional information compared to BOLD-fMRI. To do so, we derived FC matrices for resting-state ADC-fMRI and BOLD-fMRI between GM as well as WM region-of-interests (ROIs). We studied the FC in three connectivity domains (GM-GM, WM-WM and GM-WM). We then used graph analysis to study the differences between the ADC-fMRI and BOLD-fMRI networks in terms of integration and segregation, and performed an inter-subject similarity analysis to assess the consistency of FC patterns across subjects for each contrast.

2 Methods

2.1 Data acquisition

The study was approved by the Ethics Committee of the Canton of Vaud (CER-Vaud) and the dataset was previously reported on in Olszowy et al. (2021). Twenty-two subjects (7 males, age 25 $\pm$ 5) were scanned after giving their informed written consent. Siemens Prisma 3T and Siemens Magnetom 7T scanners (Siemens, Erlangen, Germany), equipped with 80 mT m^{-1} gradients, were used to acquire the data. A 64-channel and a 32-channel receiver head coils were used at 3T and 7T, respectively. Subjects were scanned at 3T and 7T in order to examine any potential field strength dependency of the ADC-fMRI functional contrast, as compared to BOLD-fMRI.

For anatomical reference and atlas registration, a whole brain 1-mm isotropic T_1-weighted image was acquired using a MP-RAGE sequence (matrix size: 224 x 240 x 256).

For rs-fMRI runs, participants were instructed to fixate on a cross in the center of a screen and to relax. Two rs-fMRI scanning protocols were used: (1) 2D multi-slice SE-EPI (T_2-BOLD contrast) and (2) 2D multi-slice DW-TRSE-EPI with alternating pairs of b-values 200 and 1000 s mm^{-2}. Spin echo (SE) BOLD was employed instead of the conventional gradient echo (GE) BOLD to allow for a more direct comparison with DW-TRSE-EPI. Note that the use of SE instead of GE for BOLD largely cancels out contributions from extravascular water around macrovasculature, increasing BOLD spatial specificity, but reducing its sensitivity (Jung & Weigel, 2013; Norris, 2012). Acquisition parameters common to both protocols were: TE: 73 ms (3T) or 65 ms (7T), TR: 1 s, matrix size: 116 x 116, 2-mm in-plane resolution, 16 x 2-mm slices, in-plane GRAPPA acceleration factor 2 (Griswold et al., 2002), partial Fourier 3/4, simultaneous multi-slice (multiband) factor 2 (Setsompop, Cohen-Adad, et al., 2012; Setsompop, Gagoski, et al., 2012), 600 volumes for a scan time of 10 min. The pairs of alternating b-values in the DW-TRSE-EPI sequence were combined to give a resulting ADC-fMRI timeseries with a TR of 2 s. The multi-band accelerated EPI sequences (http://www.cmrr.umn.edu/multiband/) were provided by

the Center for Magnetic Resonance Research (CMRR) at the University of Minnesota (Uğurbil et al., 2013). The main acquisition parameters are summarized in Supplementary Table S1.

The relatively short TR used to achieve reasonably high temporal resolution only enabled partial brain coverage (32-mm thick slab). The imaging slab (Supplementary Fig. S1) was placed to encompass part of the DMN, including the prefrontal cortex and the posterior cingulate cortex (Olszowy et al., 2021; Raichle et al., 2001). A few EPI volumes (N = 4) with opposite phase encoding direction were acquired for susceptibility distortion correction.

2.2 Data processing

The data were processed as described in Olszowy et al. (2021). (1) Slices at the extremities of the slab were excluded from the analysis due to inflow contributions (Jung & Weigel, 2013). (2) The volume outliers were automatically detected (signal dropouts) and replaced with linearly interpolated signals. For a timepoint to be considered as an outlier, the linearly detrended average signal over the entire brain should deviate by more than 1% (3T) or 3% (7T) of the median across all the timepoints. If the proportion of outlier timepoints exceeded 20%, the entire run was excluded from the analysis. For ADC-fMRI, this processing was carried out separately on b_1 and b_2 timeseries. The fraction of outliers did not exceed 5% in most of the cases. (3) MP-PCA denoising with a sliding window kernel of 5 x 5 x 5 voxels was applied on the data to boost the tSNR (Ades-Aron et al., 2021; Diao et al., 2021; Veraart et al., 2016). For ADC-fMRI, it was conducted separately on the two b-values. The residuals were checked for Gaussianity, confirming that the denoising did not alter data distribution properties. (4) Gibbs ringing correction was applied (Kellner et al., 2016). (5) Susceptibility distortions (Andersson et al., 2003) were corrected with FSL *topup*, using the settings from Alfaro-Almagro et al. (2018). (6) Motion artifacts were corrected with SPM (Penny et al., 2011). For ADC-fMRI, motion correction was performed separately on b_1 and b_2 timeseries, followed by alignment of the two series using ANTs rigid transformation (Avants et al., 2009). (7) For ADC-fMRI, ADC timeseries were obtained following equation 1. No spatial smoothing was used. (8) Independent component analysis (ICA) in FSL MELODIC (Beckmann & Smith, 2004) with high-pass temporal filtering ($f > 0.01$ Hz) and 40 independent components was used to manually identify and remove structural noise (such as motion or physiological noise) components (Diao et al., 2021; Griffanti et al., 2017). (9) Average BOLD-fMRI and ADC-fMRI timecourses were calculated in each ROI in native space using atlas-defined ROIs, described below.

2.3 Atlas registration

Brain extraction was performed using ANTs on the T_1-weighted volume before registration to the Montreal Neurological Institute (MNI) 1 mm isotropic template using symmetric normalization with ANTs. Using rigid transformation with ANTs, the average volume of each functional run was registered to the T_1-weighted anatomical volume. For ADC-fMRI, the average functional volume was calculated on the $b_1 = 200$ s mm^{-2} volumes only. The brain segmentation atlas was transformed to the subject's space using the inverse of the two previous transformations (MNI $\rightarrow$ T_1 $\rightarrow$ functional volume). The atlas used was a combination of the 1.5 mm isotropic Neuromorphometrics (NMM) gray matter atlas (*Neuromorphometrics, Inc.*, 136 ROIs) and the John Hopkins University (JHU) 1 mm isotropic white matter atlas (https://identifiers.org/neurovault.collection:264, 48 ROIs). Due to partial brain coverage, only ROIs present in all the subjects, in both contrasts (BOLD and ADC), and containing at least ten voxels were retained (Supplementary Tables S2 and S3).

2.4 Functional Connectivity

FC matrices were obtained by calculating Pearson's partial correlation between each pair of ROI timecourses, using the average timecourse of the whole brain (the global signal) as a covariate, followed by Fisher's transform. Since Global Signal Regression (GSR) may also remove relevant functional signal and alter the distribution of correlation coefficients (Schölvinck et al., 2010), we duplicated the analysis without GSR to test the robustness of the results. FC matrices were finally averaged across subjects for each contrast.

2.5 Graph analysis

Only significant positive correlations in individual FC matrices were considered, determined with two-sided one-sample Wilcoxon tests with multiple comparisons correction (FDR Benjamini-Hochberg, Benjamini and Hochberg 1995). Weighted metrics for testing the network strength (average node strength), segregation (average clustering) and integration (global efficiency) were calculated for each subject. The detailed formula of the weighted metrics can be found in Rubinov and Sporns (2010).

The node strength corresponds to the sum of the connection weights for a given node (the weighted equivalent of the node degree), averaged across all nodes to yield average node strength for the network (Rubinov & Sporns, 2010).

The clustering coefficient of a node is a measure of inter-connectivity (local functional connectivity) between its neighboring nodes (Farahani et al., 2019; Sporns et al., 2004; Watts & Strogatz, 1998). The clustering coefficient of a network (averaged across nodes) indicates the level of clustered connectivity around individual nodes, thus it is a measure of network segregation (Rubinov & Sporns, 2010; Watts & Strogatz, 1998).

The global efficiency is the average of the inverse shortest path length between all pairs of nodes, where path lengths are defined inversely to FC. Shorter paths between nodes indicate a high possibility of information flow across the brain, therefore a higher efficiency corresponds to enhanced potential for integration (Rubinov & Sporns, 2010).

2.6 Statistical Analysis

The regression lines between FC values derived from each contrast were measured for positive and negative group-mean edge weights separately.

Significant positive and negative FC weights within each contrast were determined with two-sided one-sample Wilcoxon tests with multiple comparisons correction (FDR Benjamini-Hochberg, Benjamini and Hochberg 1995). These significant connections were then split according to their connectivity domains (GM-GM, WM-WM, GM-WM). To assess differences between ADC-fMRI and BOLD-fMRI, we compared significant FC edges in each domain using two-sided Mann-Whitney-Wilcoxon tests, with Bonferroni correction for multiple comparisons.

We also compared the ADC-fMRI and BOLD-fMRI graph metrics in the GM-GM and in the WM-WM domains using two-sided Mann-Whitney-Wilcoxon tests, with Bonferroni correction for multiple comparisons.

Finally, the pairwise inter-subject similarity within each contrast was derived by calculating the Pearson correlation coefficients between the significant GM-GM, WM-WM, or GM-WM edges, excluding self-connections.

3 Results

The analysis was performed on data acquired at 3T and 7T, separately. As both field strengths led to similar results and interpretations, only the 3T results are discussed here while the 7T results can be

found in the supplementary materials.

3.1 Functional connectivity

3.1.1 GM-GM connectivity

At 3T, FC matrices (Supplementary Fig. S2) yielded similar positive correlations between ADC-fMRI and BOLD-fMRI, with BOLD-fMRI displaying overall larger mean positive correlations in the GM-GM connectivity. Regions corresponding to the DMN were typically positively correlated for both ADC-fMRI and BOLD-fMRI. For instance, the anterior cingulate gyrus (ACgG) was positively correlated with the medial frontal cortex (MFC) and the superior frontal gyrus medial segment (MSFG), while the superior frontal gyrus (SFG) was positively correlated with the medial frontal gyrus (MFG), the MSFG and the frontal pole (FRP). BOLD-fMRI also displayed larger negative correlations than ADC-fMRI. In particular, the middle temporal gyrus (MTG) and superior temporal gyrus (STG) negatively correlated with the MSFG and the ACgG.
At 7T, similar positive correlations were visible in ADC-fMRI and BOLD-fMRI (Supplementary Fig. S3). The negative correlations were greatly attenuated in ADC-fMRI, but appeared strongly in BOLD-fMRI, especially in the GM-GM. The negative correlations of ADC-fMRI also appeared between the MTG/STG and the ACgG/MSFG.

3.1.2 GM-WM connectivity

At 3T, in ADC-fMRI, the splenium of the corpus callosum (sCC) was negatively correlated with the ACgG and the MFC, but positively correlated with the posterior cingulate gyrus (PCgG). In BOLD-fMRI, the sCC was also positively correlated with the PCgG, while the tapetum (TAP) was negatively correlated with the MSFG. In both ADC-fMRI and BOLD-fMRI, the anterior part of the corona radiata (ACR) was positively correlated with the ACgG (Karababa et al., 2015; Wakana et al., 2004).
At 7T, the genu of the corpus callosum (gCC) and the ACR were positively correlated with the ACgG in both contrasts. Finally, the cingulum (hippocampus) (CgH) was negatively correlated with the triangular part of inferior frontal gyrus (TrIFG) in BOLD-fMRI.

3.1.3 WM-WM connectivity

At 3T, in both contrasts, the gCC was positively correlated with the ACR. In addition, the posterior thalamic radiation (PTR) was positively correlated with the superior longitudinal fasciculus (SLF).
At 7T, the same association between gCC and ACR was found. With ADC-fMRI, positive FC between the external capsule (EC) and the anterior/posterior limb of the internal capsule (ALIC/PLIC) and between the fornix (cres)/stria terminalis (FX/ST) and the sagittal stratum (SS) were also found.

To further check the congruence between ADC-fMRI and BOLD-fMRI, we compared the connectivity strength of ADC-fMRI edges with the corresponding BOLD-fMRI edges **at 3T** as proposed by Olszowy et al. (2021), but this time extending the analysis to GM-WM and WM-WM edges (Fig. 1).

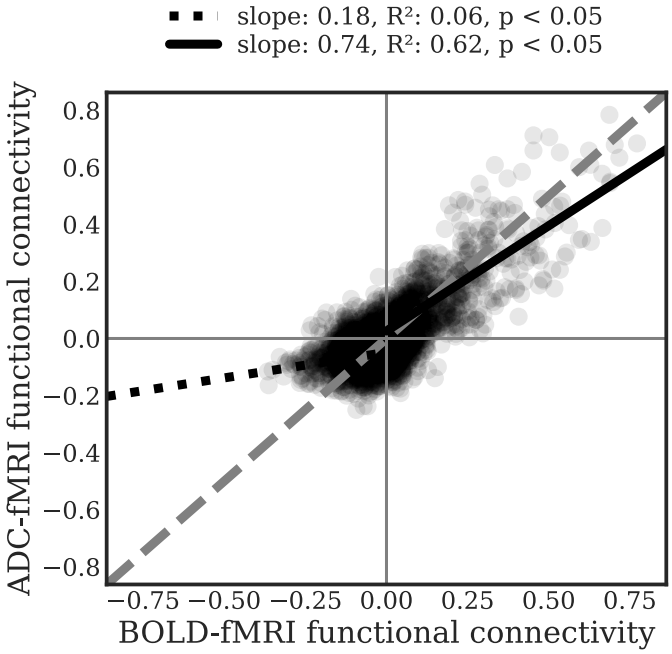

Figure 1: **ADC-to-BOLD agreement of mean FC strength at 3T**, between corresponding edges. The solid line fits the positive correlations, while the dotted line fits the negative correlations. The dashed line represents a perfect agreement (identity line). Functional connectivity strength is defined as Fisher-transformed Pearson's correlation coefficient. There is excellent agreement between ADC-fMRI and BOLD-fMRI positive FC, while BOLD-fMRI negative FC is largely suppressed in ADC-fMRI.

For the positive functional connections, the linear fit between ADC-fMRI and BOLD-fMRI had a slope of 0.74 and a R^2 of 0.62. For the negative functional connections, the fit had a slope of 0.18 but a R^2 of 0.06.
The same analysis was conducted **at 7T** with similar results (Supplementary Fig. S4). When performed without GSR, the excellent agreement between ADC-fMRI and BOLD-fMRI positive FC remained, while the disagreement in negative FC was not possible to assess anymore due to a near absence of negative

edges (Supplementary Fig. S9).

To gain more specific insight into the distribution of positive and negative FC in the GM-GM, WM-WM and GM-WM connectivity, we further segmented the data based on these specific domains (Fig. 2).

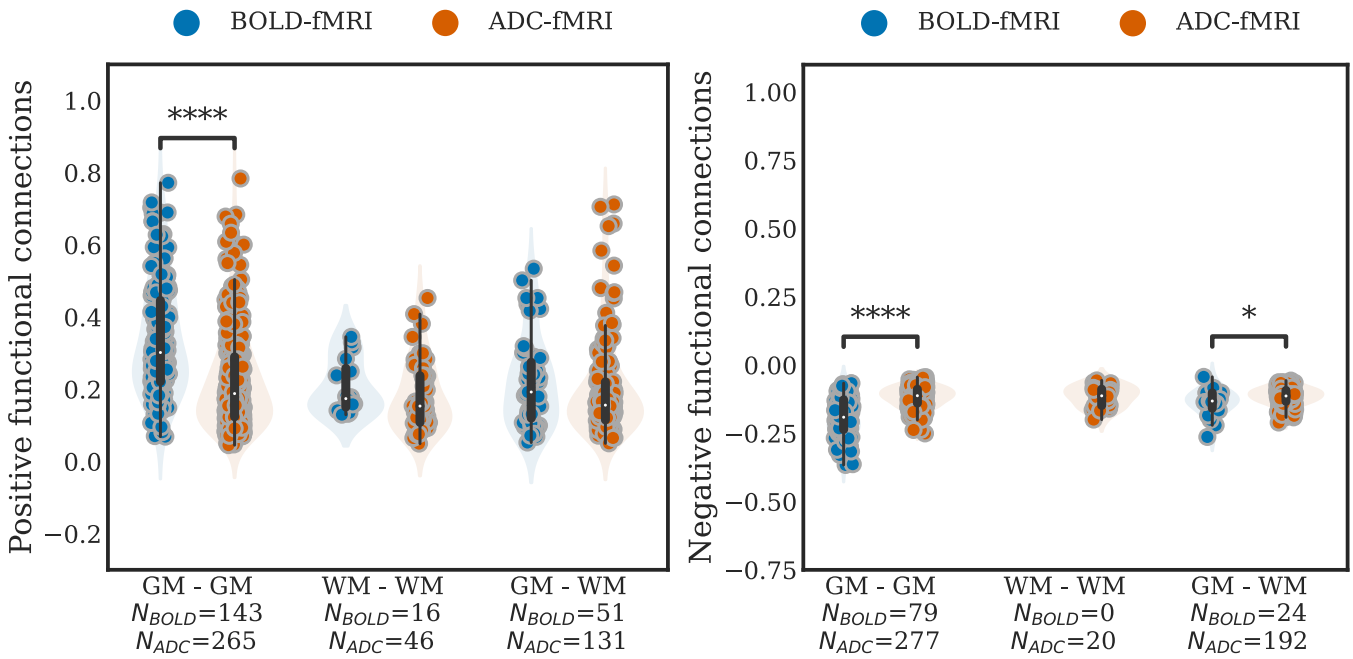

(A) Positive functional connections (B) Negative functional connections

Figure 2: **Significant positive and negative functional connections at 3T**, for BOLD-fMRI and ADC-fMRI. The correlations are split by tissue type (GM-GM, WM-WM, and GM-WM connectivity). **(A)** Positive correlations, **(B)** negative correlations. The number of significant edges per functional contrast is indicated on the x-axis label. No negative correlations were found for BOLD-fMRI WM-WM. Two-sided Mann-Whitney-Wilcoxon tests with Bonferroni correction are performed. * $0.01 < p \leq 0.05$; ** $10^{-3} < p \leq 0.01$; *** $10^{-4} < p \leq 10^{-3}$; **** $p \leq 10^{-4}$.

At 3T, positive FC was indeed significantly stronger for BOLD-fMRI than for ADC-fMRI in the GM-GM, supporting the visual inspection (Fig. 2A). In WM-WM and in GM-WM, no differences were found in positive connections between the two contrasts. For the negative connections, they were significantly attenuated in ADC-fMRI in the GM-GM and GM-WM (Fig. 2B), but no anti-correlations were found for BOLD-fMRI in the WM-WM.

At 7T, positive FC was also significantly stronger for BOLD-fMRI than ADC-fMRI in the GM-GM (Supplementary Fig. S5A). In the WM-WM, the positive connections were significantly greater for ADC-fMRI vs BOLD-fMRI, but no differences were found in the GM-WM positive connections between the two contrasts. For the negative connections, they were significantly attenuated in ADC-fMRI in the GM-GM (Supplementary Fig. S5B), but no anti-correlations were found for BOLD-fMRI in the WM-WM.

At 3T without GSR, positive connections were still significantly larger in BOLD-fMRI than ADC-fMRI

in the GM-GM (Supplementary Fig. S10A) while significantly larger in ADC-fMRI than BOLD-fMRI in the WM-WM and in the GM-WM. Negative FC was almost non-existent. In all cases (at 3T, 7T and 3T without GSR) except in the GM-WM negative FC at 3T without GSR, the number of significant positive and negative edges detected with ADC-fMRI was larger than with BOLD-fMRI.

3.2 Graph Analysis

Following the analysis of individual FC edges, we then studied the networks formed by the GM-GM and WM-WM parts of the FC matrices. Several graph metrics were computed and compared between the two contrasts.

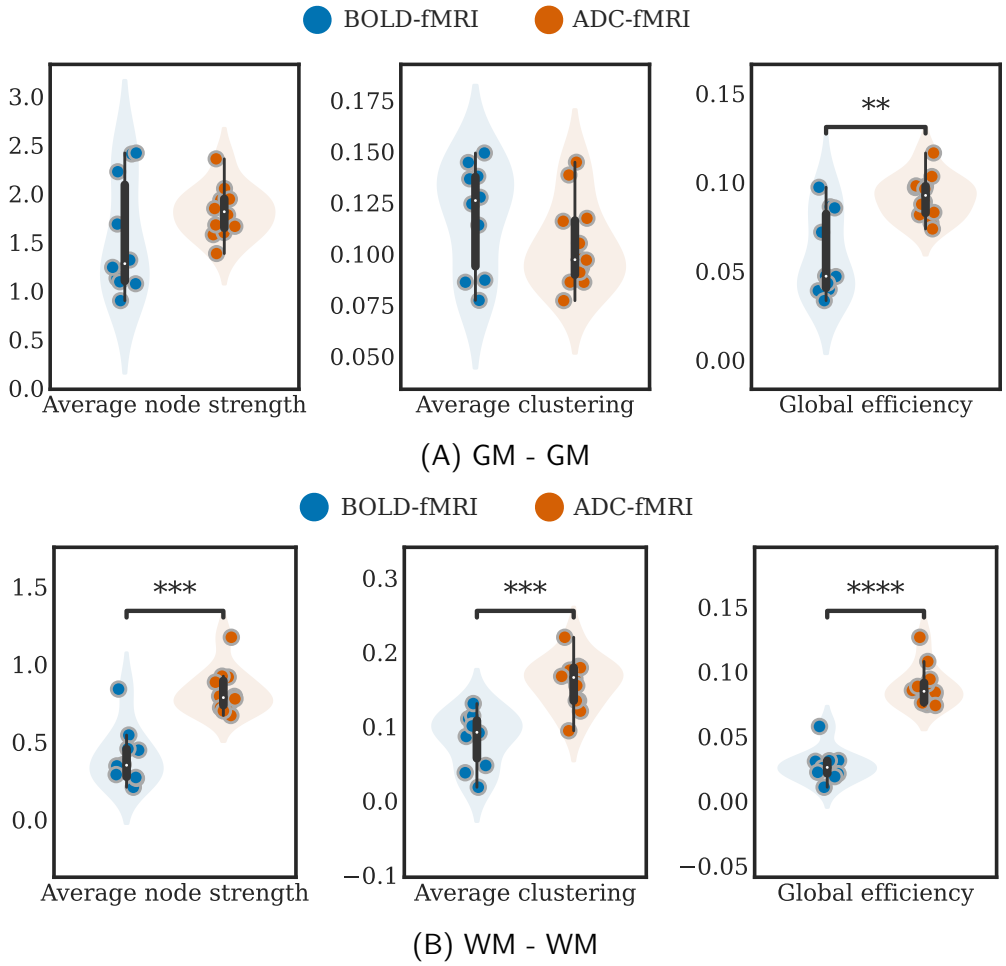

Figure 3: **Weighted graph metrics at 3T**, calculated for BOLD-fMRI (n = 10) and ADC-fMRI (n = 12). **(A)** Graph metrics based on the GM-GM connectivity. **(B)** Graph metrics based on the WM-WM connectivity. Two-sided Mann-Whitney-Wilcoxon tests with Bonferroni correction were performed. * $0.01 < p \leq 0.05$; ** $10^{-3} < p \leq 0.01$; *** $10^{-4} < p \leq 10^{-3}$; **** $p \leq 10^{-4}$.

At 3T, in the GM-GM, the average clustering and average node strength were similar between ADC-fMRI and BOLD-fMRI (Fig. 3A). They were however significantly larger for ADC-fMRI than BOLD-fMRI for networks built on WM-WM connectivity (Fig. 3B). The global efficiency was significantly larger for ADC-fMRI in both the GM-GM and WM-WM connectivity.

At 7T, the average node strength and global efficiency were similar in the GM-GM (Supplementary Fig. S6A), but became significantly larger in ADC-fMRI in the WM-WM (Supplementary Fig. S6B). The average clustering was significantly larger in BOLD-fMRI in the GM-GM, but significantly larger in ADC-fMRI in the WM-WM.

At 3T, without GSR, all graph metrics were similar between ADC-fMRI and BOLD-fMRI in the GM-GM (Supplementary Fig. S11A) but the average node strength and clustering remained significantly larger for ADC-fMRI vs BOLD-fMRI in the WM-WM (Supplementary Fig. S11B).

3.3 Inter-subject similarity

Finally, we assessed the consistency of FC patterns across subjects by computing inter-subject similarity matrices for both ADC-fMRI and BOLD-fMRI data, in the different connectivity domains (Fig. 4). **At 3T**, the consistency across subjects (measured as pairwise Pearson correlation of the vectorized FC matrices) was larger for ADC-fMRI (mean 0.70, 95% CI [0.68, 0.72]) than for BOLD-fMRI (0.38 [0.31, 0.44]) in the WM-WM. Note that the number of significant edges N_e used to calculate the pairwise correlation between two subjects was systematically larger for ADC-fMRI than BOLD-fMRI. A similar analysis was therefore performed on all edges ($N_e = 210$ in both contrasts) to ensure that the significant difference in the WM-WM inter-subject similarity between ADC-fMRI and BOLD-fMRI was not biased by the small sample size (Supplementary Fig. S8). In this case, the ADC-fMRI inter-subject similarity was still larger (0.52 [0.50, 0.55]) than the BOLD-fMRI similarity (0.42 [0.38, 0.47]).

At 7T, the inter-subject similarity was larger for ADC-fMRI than for BOLD-fMRI in all the connectivity regions (Supplementary Fig. S7). Consistent with the 3T findings, the mean WM-WM inter-subject similarity was 0.67 [0.64, 0.70] for ADC-fMRI, but 0.24 [0.18, 0.31] for BOLD-fMRI.

4 Discussion

Although resting-state FC that includes both gray and white matter regions has been occasionally studied using BOLD-fMRI (J. Li, Biswal, et al., 2019), this work is the first to assess ADC-fMRI resting-state FC in gray and white matter, and compare it to its BOLD-fMRI counterpart. We found that the positive

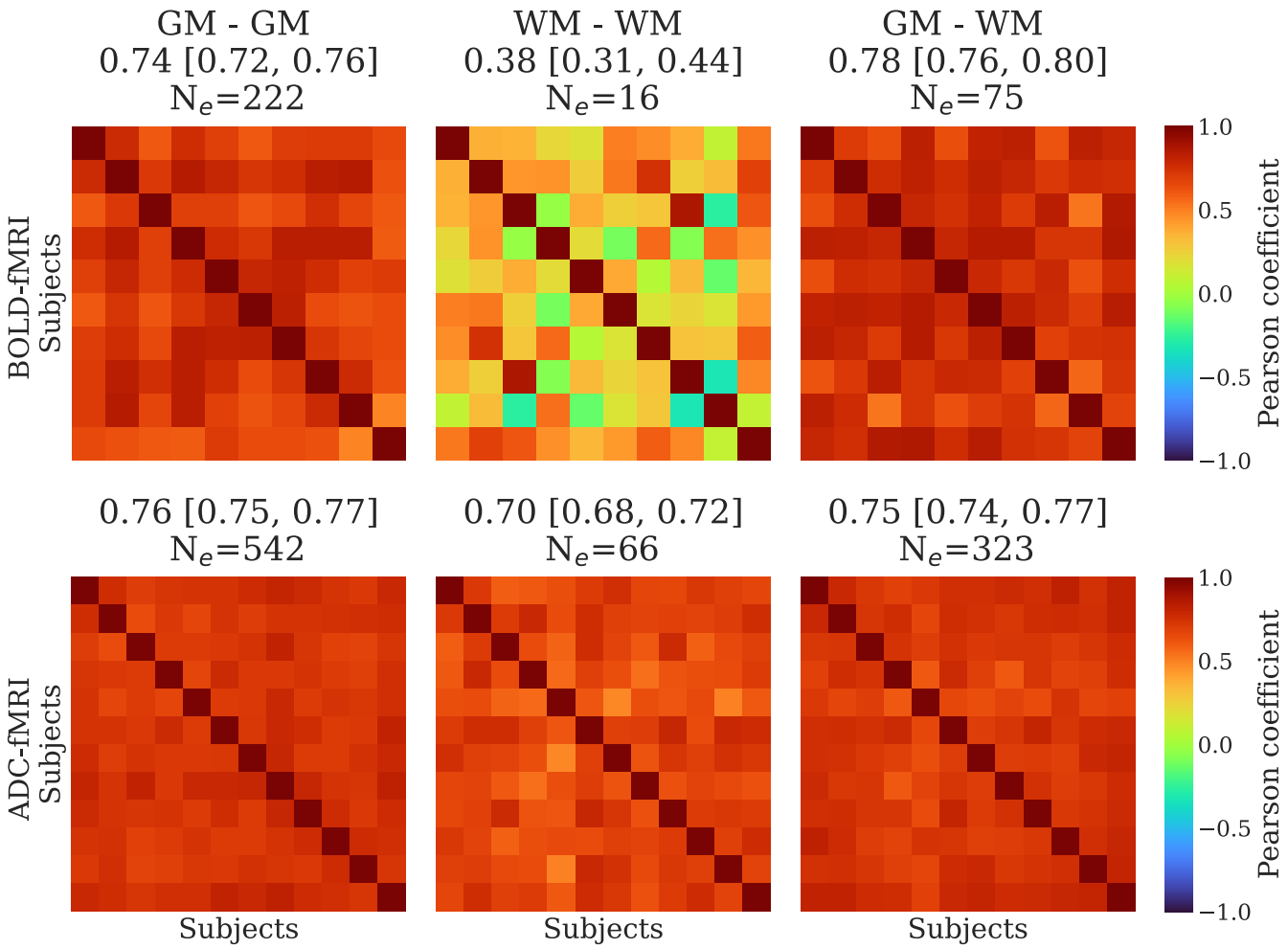

Figure 4: **Inter-subject FC similarity at 3T** of the significant edges for BOLD-fMRI and ADC-fMRI, calculated as the pairwise Pearson correlation of the vectorized FC matrices. Each similarity matrix has a size $N_{subjects}$ x $N_{subjects}$, with $N_{BOLD-fMRI} = 10$ and $N_{ADC-fMRI} = 12$. The mean Pearson's correlation coefficient of the similarity matrix and the 95% CI are depicted in the subtitles. N_e corresponds to the number of FC significant edges on which the Pearson's correlation coefficients are calculated. The GM-GM, WM-WM and GM-WM connectivity were considered separately.

FC was extremely well preserved between ADC-fMRI and BOLD-fMRI, while negative FC was heavily attenuated in ADC-fMRI. We then investigated the positive and negative FC in different types of brain tissue. We found that both positive FC in the GM-GM and negative FC in all domains had a larger magnitude in BOLD-fMRI than in ADC-fMRI. While the positive FC results still held without GSR, the negative FC did not survive the statistical tests. In addition, we characterized the networks using weighted graph metrics (average clustering, average node strength and global efficiency). We found that the average node strength and the average clustering were significantly larger for ADC-fMRI than BOLD-fMRI in the WM-WM, while this difference was not significant in the GM-GM. Finally, we tested the inter-subject similarity and found that it was larger in ADC-fMRI vs BOLD-fMRI, particularly for

WM-WM connectivity, suggesting a higher reproducibility of ADC-fMRI FC in that domain.

4.1 ADC-fMRI retains BOLD-fMRI positive functional connections in gray matter

ADC-fMRI and BOLD-fMRI positive FC mirrored each other, both with their mean FC strength (as previously noted in Olszowy et al. 2021) and their weighted graph metrics (average node strength and clustering). Overall, positive FC was larger in BOLD-fMRI than ADC-fMRI, due to its higher CNR, particularly in GM. We further extended this analysis to individual edges and found that the DMN stood out, as expected during a resting state acquisition. Forming the anterior DMN, the ACgG, MSFG, FRP and SFG have high FC to each other (Xu et al., 2016). Moreover, positive FC was also found between ACgG and MFC (Cao et al., 2014). Together, these established connections provide additional assurance of the high correspondence of positive functional connections between ADC-fMRI and BOLD-fMRI positive FC, and confirm that ADC-fMRI is a reliable tool to decipher resting-state connectivity in the GM.

4.2 Does ADC-fMRI attenuate anti-correlations?

Conversely, negative correlations are more difficult to interpret. In this work, we found negative FC between MTG and MSFG/ACgG for BOLD-fMRI, as previously described in a similar analysis also performed with GSR (Fox et al., 2009). In addition, we observed BOLD negative correlations between the sCC and ACgG/MFC, between the TAP and the MSFG, as well as between the CgH and the TrIFG, as reported in a study not using GSR (Ding et al., 2018). We also found these negative correlations in ADC-fMRI, indicating that both neurovascular and neuromorphological contrasts are sensitive to these negative correlations and that the latter may have a physiological significance. It is known that task-positive networks (showing increased activity during task execution) negatively correlate with task-negative networks (showing reduced activity during task execution, such as the DMN), suggesting an inhibitory interaction between both antagonist networks (Bianciardi et al., 2011; Fox et al., 2005). However, in our analysis, almost all negative correlations disappeared when performed without GSR. Earlier studies showed that negative correlations could be mainly GSR-driven (Murphy et al., 2009; Weissenbacher et al., 2009), introducing artefactual negative correlations, while other studies showed GSR to improve FC specificity when used with care (Chai et al., 2012; Fox et al., 2009; J. Li, Kong, et al., 2019; Murphy & Fox, 2017). More and more studies are reporting their results with and without GSR, finding negative correlations in both cases (Chai et al., 2012; Chen et al., 2011). Another explanation could be that, in the same way

the global signal fluctuations mask established neuronal associations concerning positive correlations, they could also obscure negative correlations in BOLD-fMRI FC (Fox et al., 2009). In this work, they were largely absent or attenuated in ADC-fMRI in spite of an analysis pipeline identical to BOLD-fMRI, including GSR. If GSR was inducing negative correlations, we would expect it to cause similar changes to both ADC-fMRI and BOLD-fMRI. In addition, in Ding et al. (2018), the analysis was performed without GSR, which suggests that anti-correlations are not necessarily artifactual.

The preferential attenuation of anti-correlations in ADC-fMRI vs BOLD-fMRI suggests that part of the negative correlations have a vascular origin. Adding to this, in the WM, where the vasculature is largely reduced, no anti-correlations were found for BOLD-fMRI. Bianciardi et al. (2011) supported this hypothesis by reporting that blood volume changes may also induce negative correlations, especially in periventricular regions, as well as sulcal areas next to large pial veins. Anti-correlations can however also be caused by noise sources such as motion or physiological variations.

4.3 ADC-fMRI is more sensitive to white matter functional connectivity than BOLD-fMRI

Initially thought to be driven by physiological noise, the BOLD-fMRI WM signal is increasingly recognized as consisting of hemodynamic changes reflecting neural activity in the WM or in neighboring GM regions, although with reduced sensitivity (Gore et al., 2019; Grajauskas et al., 2019). In this work, we compared for the first time BOLD-fMRI and ADC-fMRI derived GM-WM and WM-WM connectivity.

4.3.1 Gray to white matter connectivity

Few studies have considered GM-WM connectivity. Ding et al. (2018) reported positive and negative BOLD-fMRI GM-WM correlations at 3T. Remarkably, our study revealed similar positive and negative BOLD-fMRI correlations to Ding et al. (2018) at 3T (but also at 7T), which strengthens the viability of BOLD-fMRI to study ROI-based GM-WM connectivity. Moreover, most of the BOLD-derived GM-WM connectivity patterns were also found using ADC-fMRI. This suggests that ADC-fMRI is also a suitable tool to detect positive and negative FC in the GM-WM edges.

M. Li et al. (2019) derived BOLD HRFs for superficial, middle and deep WM. They found that the BOLD HRF corresponding to superficial WM was similar to the BOLD GM HRF, possibly allowing correlation analysis between WM and GM timecourses. However, they reported that middle and deep WM HRFs could display an additional delay to peak, possibly due to the different nature and distance of the blood

vessels (M. Li et al., 2019). Taken together, the heterogeneity of the WM HRFs, if confirmed, could bring an additional challenge to deriving GM-WM functional connectivity. We hypothesize that BOLD-derived WM-GM FC analysis will be mostly sensitive to the superficial WM.

4.3.2 White to white matter connectivity

Similarly to GM-WM, WM-WM connectivity has been scarcely studied (J. Li, Biswal, et al., 2019). Here, we found that BOLD-fMRI sensitivity was reduced for the exploration of WM-WM connectivity, possibly due to the reduced low frequency oscillations, blood flow and blood volume in the WM (Biswal et al., 1995; Gore et al., 2019). For instance, positive FC values were significantly larger for ADC-fMRI than BOLD-fMRI in WM-WM at 7T. Further looking into the graph metrics analysis, we found larger average clustering coefficients and average node strength in ADC-fMRI than in BOLD-fMRI in the WM-WM connectivity, suggesting the two functional contrasts capture different connectivity aspects in the WM. Global efficiency was larger in ADC-fMRI than in BOLD-fMRI in both WM-WM and GM-GM at 3T, but particularly in the WM-WM. Differences in graph metrics may be driven by ADC-fMRI robustness to physiological noise in the GM-GM and by decreased BOLD-fMRI sensitivity in the WM-WM. Taken together, the ADC-fMRI network metrics reflected both better integration and segregation in the WM than BOLD-fMRI. Because GSR can impact FC values by shifting them towards more negative values, it can ultimately impact network metric calculations. Indeed, the networks on which the metrics were calculated ignored negative FC values. This selection of positive FC edges may affect the BOLD-fMRI and ADC-fMRI graph metrics differently due to different distributions of positive and negative correlations. Therefore, we compared graph metrics derived from ADC-fMRI vs BOLD-fMRI FC also without GSR, but found similar results, as also observed in J. Li, Biswal, et al. (2019). This suggests that the graph metric differences between the two functional contrasts are not driven by GSR-induced biases.

Remarkably, our data also showed that ADC-fMRI has a higher between-subject similarity than BOLD-fMRI in the WM-WM connectivity. This suggests that ADC-fMRI is more consistent across subjects, possibly due to attenuation of physiological noise thanks to the "self-normalization" inherent to the ADC calculation from two consecutive diffusion-weighted images. It cancels out not only T2-weighting but also fluctuations due to respiratory and cardiac motion, for example. Alternatively, the lower BOLD-fMRI inter-subject similarity could reflect the fact that BOLD-fMRI is more sensitive to inter-subject differences and is able to detect individual fingerprinting (Finn et al., 2015). The latter is however more unlikely, as the BOLD-fMRI similarity coefficients are high in edges other than WM-WM. Taken together, ADC-fMRI revealed consistent patterns of WM-WM connectivity, making it a useful tool for investigating WM functional connectivity.

4.4 ADC-fMRI is not a vascular contrast

As mentioned in the introduction, the underlying mechanism of the ADC-fMRI contrast is debated. While its advocates support the consensus that ADC fluctuations are driven by activity-induced neuromorphological changes, its critics claim that this contrast is either contaminated by the hemodynamic response or driven by morphological changes induced by vascular dilation (Jin & Kim, 2008; Jin et al., 2006). In this work, we have shown that ADC-fMRI does not mimic BOLD, but is indeed a separate contrast. Notably, negative FC patterns were distinct between ADC-fMRI and BOLD-fMRI, negative correlations being highly attenuated in ADC-fMRI. In addition, the WM connectivity captured by both contrasts was significantly different, both in terms of graph metrics, but also in terms of consistency across subjects. While ADC-fMRI WM-WM connectivity was consistent across subjects, BOLD-fMRI WM-WM connectivity varied much more. Thanks to the mitigation techniques implemented in this study, ADC-fMRI is much more robust to physiological noise and vascular contributions. Therefore, the higher number of significant edges found in ADC-fMRI across connectivity regions (GM-GM, GM-WM, WM-WM) could also stem from robustness against physiological noise. At 3T, the higher number of subjects for ADC-fMRI ($n = 12$) than BOLD-fMRI ($n = 10$), probably also increased the number of significant edges found in ADC-fMRI. However at 7T, despite the same sample size ($n = 10$), ADC-fMRI still detected more significant edges than BOLD-fMRI in all connectivity regions, supporting the hypothesis that ADC-fMRI FC is more robust to physiological noise.

Our results were therefore in line with previous studies that aimed to untangle neuromorphological from vascular effects, using targeted inhibition of key physiological processes following neuronal activity. Disrupting the hemodynamic response, aquaporin-4 blocker (Komaki et al., 2020) and nitroprusside (Tsurugizawa et al., 2013) were used in mice and rats, respectively. In both cases, the BOLD response was notably affected while the ADC was not. Regarding neuromorphological effects, cell swelling induced via hypotonic solution or ouabain was shown to decrease ADC at the tissue level (Jelescu et al., 2014), albeit outside of physiological ranges. Conversely, Abe et al. (2017) showed that the ADC increased under the effect of the neural swelling blocker furosemide during anesthesia while the local field potentials (LFPs) remained unaffected. Our results provided additional support for the non-vascular origins of ADC changes during neuronal activity. Preclinical studies suggested these changes could be driven by fluctuations in cell shapes and sizes, as ADC is so sensitive to the microstructure layout. Other mechanisms cannot however be entirely ruled out.

4.5 ADC-fMRI vs field strength

By paralleling the analysis at 3T and 7T, we wanted to verify the influence of the field strength on each of the two functional contrasts. The magnitude of the BOLD signal is known to scale with field strength (Barth & Poser, 2011; Gati et al., 1997), whereas we hypothesized that the magnitude of the ADC response should be independent of field strength, if stemming from neuromorphological coupling. However, field strength dependencies are complex and affect each functional contrast in multiple ways. For example, the SNR and the ratio of physiological to thermal noise increase with field strength (Barth & Poser, 2011). In addition, due to the shortening of blood T_2 with increasing field strength, the BOLD signal contains less direct intravascular component, and therefore has increased spatial specificity. In contrast, ADC-fMRI timecourses are less sensitive to physiological noise but ADC FC analysis could benefit from higher SNR at higher field. However, mitigating vascular contributions to the ADC timecourse may be more difficult at 7T due to increased magnetic susceptibility (Olszowy et al., 2021). In the context of resting-state fMRI, our results were similar at 3T and 7T, but the dependence of ADC-fMRI on field strength may become apparent in task-fMRI.

4.6 Limitations

The small sample size is one of the main limitations of this study. It diminished the statistical power of the analyses, highlighting the need for future studies with larger sample sizes. In addition, to optimize spatial and temporal resolution, only a section of the brain was scanned (a partial coverage which was further reduced when coregistering subjects to a common space due to slight variations in slab positioning), which limited the extent of functional connectivity that could be examined across the brain. Furthermore, the use of two b-values to calculate one ADC-fMRI timepoint resulted in a lower temporal resolution (2 s) for ADC-fMRI, possibly leading to the aliasing of faster physiological processes, whether related to brain activity or to other signals such as respiration and heart signal (Lund et al., 2006). Additionally, DW-TRSE-EPI used in this study was only acquired using one diffusion encoding direction. This possibly yields an inhomogeneous sensitivity to neuromorphological changes across the brain, depending on the angle between the main fibers at each location and the diffusion encoding direction, with expected higher sensitivity for fibers perpendicular to that direction and lower for fibers parallel to that direction. Lastly, even though the use of spin-echo BOLD rather than gradient-echo BOLD sequence enabled a fair comparison with the DW-TRSE sequence, spin-echo BOLD exhibits less sensitivity than gradient-echo BOLD, possibly missing some of the resting-state BOLD characteristics described in the literature.

4.7 Perspectives

To overcome the partial brain coverage, additional acceleration in diffusion MRI acquisition needs to be introduced to acquire a large number of slices within a short TR, possibly using novel undersampling strategies (Setsompop et al., 2018). This would enable a more comprehensive comparison of GM-WM correlations as presented in Ding et al. (2018), as well as WM-WM. In addition, the temporal resolution could be increased by using a sliding window to calculate an ADC at each TR, although this is expected to introduce temporal auto-correlations and may not yield more informative ADC timecourses. In future studies, isotropic diffusion encoding will be used to sensitize ADC-fMRI to fibers no matter their orientation (Spencer et al., 2024). ADC-fMRI FC could even be used in combination with structural tractography as a way to track neuronal activity along white matter fibers, up to the cortical areas.

5 Conclusions

This study indicates that ADC-fMRI is a promising tool for resting-state analysis. It retained comparable positive correlations to BOLD-fMRI in the GM. Most interestingly, ADC-fMRI showed clearly distinct functional contrast from neurovascular coupling, notably via largely reduced anti-correlations in GM. Furthermore, larger average clustering coefficients, average node strength and global efficiency in the WM-WM connectivity as compared to BOLD-fMRI, combined with higher inter-subject similarity in the WM-WM, suggest that ADC-fMRI has a high sensitivity and robustness to WM functional connectivity. In the future, it holds great potential for elucidating WM functional connectivity as an alternative to BOLD-fMRI. Future work will use an isotropic diffusion encoding to sensitize the ADC-fMRI in all directions, thus preventing bias towards fibers perpendicular to the diffusion encoding direction.

Data and code availability

The Matlab code used to process the data is available on https://github.com/Mic-map/DfMRI. The python code used to run the analyses is available at https://github.com/Mic-map/ADC_rsfMRI. The data will be available upon publication.

Author contributions

Conceptualization: I.J., I.d.R.; Methodology: I.J., I.d.R., A.S.; Validation: I.d.R.; Formal analysis: I.d.R.; Investigation: W.O.; Data curation: W.O., I.d.R.; Writing-original draft: I.d.R.; Writing - Review & Editing: I.d.R., I.J., W.O., A.S.; Visualization: I.d.R.; Supervision: I.J.; Funding acquisition: I.J.

Funding

This work was supported by the Swiss National Science Foundation under a Spark award CRSK-2_190882 and by the Swiss Secretariat for Research and Innovation (SERI) under an ERC Starting Grant award 'FIREPATH' MB22.00032.

Declaration of Competing Interest

All authors declare no competing interests.

Acknowledgements

The authors thank Thomas Bolton and Jasmine Nguyen-Duc for insightful discussions. They acknowledge the CIBM Center for Biomedical Imaging for providing expertise and resources to conduct this study.

References

Abe, Y., Takata, N., Sakai, Y., Hamada, H. T., Hiraoka, Y., Aida, T., Tanaka, K., Bihan, D. L., Doya, K., & Tanaka, K. F. (2020). Diffusion functional MRI reveals global brain network functional abnormalities driven by targeted local activity in a neuropsychiatric disease mouse model. *NeuroImage*, *223*, 117318. https://doi.org/10.1016/j.neuroimage.2020.117318

Abe, Y., Tsurugizawa, T., & Le Bihan, D. (2017). Water diffusion closely reveals neural activity status in rat brain loci affected by anesthesia. *PLoS Biology*, *15*(4), e2001494. https://doi.org/10.1371/journal.pbio.2001494

Ades-Aron, B., Lemberskiy, G., Veraart, J., Golfinos, J., Fieremans, E., Novikov, D. S., & Shepherd, T. (2021). Improved Task-based Functional MRI Language Mapping in Patients with Brain Tumors through Marchenko-Pastur Principal Component Analysis Denoising. *Radiology*, *298*(2), 365–373. https://doi.org/10.1148/radiol.2020200822

Alfaro-Almagro, F., Jenkinson, M., Bangerter, N. K., Andersson, J. L. R., Griffanti, L., Douaud, G., Sotiropoulos, S. N., Jbabdi, S., Hernandez-Fernandez, M., Vallee, E., Vidaurre, D., Webster, M., McCarthy, P., Rorden, C., Daducci, A., Alexander, D. C., Zhang, H., Dragonu, I., Matthews, P. M., . . . Smith, S. M. (2018). Image processing and Quality Control for the first 10,000 brain imaging datasets from UK Biobank. *NeuroImage*, *166*, 400–424. https://doi.org/10.1016/j.neuroimage.2017.10.034

Andersson, J. L. R., Skare, S., & Ashburner, J. (2003). How to correct susceptibility distortions in spin-echo echo-planar images: Application to diffusion tensor imaging. *NeuroImage*, *20*(2), 870–888. https://doi.org/10.1016/S1053-8119(03)00336-7

Avants, B. B., Tustison, N., Song, G., et al. (2009). Advanced normalization tools (ants). *Insight j*, *2*(365), 1–35.

Babaeeghazvini, P., Rueda-Delgado, L. M., Gooijers, J., Swinnen, S. P., & Daffertshofer, A. (2021). Brain Structural and Functional Connectivity: A Review of Combined Works of Diffusion Magnetic Resonance Imaging and Electro-Encephalography. *Frontiers in Human Neuroscience*, *15*. Retrieved March 1, 2024, from https://www.frontiersin.org/articles/10.3389/fnhum.2021.721206

Bai, R., Stewart, C. V., Plenz, D., & Basser, P. J. (2016). Assessing the sensitivity of diffusion MRI to detect neuronal activity directly. *Proceedings of the National Academy of Sciences*, *113*(12), E1728–E1737. https://doi.org/10.1073/pnas.1519890113

Bammer, R. (2003). Basic principles of diffusion-weighted imaging. *European Journal of Radiology*, *45*(3), 169–184. https://doi.org/10.1016/S0720-048X(02)00303-0

Barth, M., & Poser, B. A. (2011). Advances in High-Field BOLD fMRI. *Materials*, *4*(11), 1941–1955. https://doi.org/10.3390/ma4111941

Beckmann, C., & Smith, S. (2004). Probabilistic independent component analysis for functional magnetic resonance imaging. *IEEE Transactions on Medical Imaging*, *23*(2), 137–152. https://doi.org/10.1109/TMI.2003.822821

Benjamini, Y., & Hochberg, Y. (1995). Controlling the False Discovery Rate: A Practical and Powerful Approach to Multiple Testing. *Journal of the Royal Statistical Society. Series B (Methodological)*, *57*(1), 289–300. Retrieved March 5, 2024, from https://www.jstor.org/stable/2346101

Bianciardi, M., Fukunaga, M., van Gelderen, P., de Zwart, J. A., & Duyn, J. H. (2011). Negative BOLD-fMRI signals in large cerebral veins. *Journal of Cerebral Blood Flow & Metabolism*, *31*(2), 401–412. https://doi.org/10.1038/jcbfm.2010.164

Biswal, B., Yetkin, F. Z., Haughton, V. M., & Hyde, J. S. (1995). Functional connectivity in the motor cortex of resting human brain using echo-planar MRI. *Magnetic Resonance in Medicine*, *34*(4), 537–541. https://doi.org/10.1002/mrm.1910340409

Cao, W., Luo, C., Zhu, B., Zhang, D., Dong, L., Gong, J., Gong, D., He, H., Tu, S., Yin, W., Li, J., Chen, H., & Yao, D. (2014). Resting-state functional connectivity in anterior cingulate cortex in normal aging. *Frontiers in Aging Neuroscience*, *6*. Retrieved February 14, 2024, from https://www.frontiersin.org/articles/10.3389/fnagi.2014.00280

Chai, X. J., Castañón, A. N., Öngür, D., & Whitfield-Gabrieli, S. (2012). Anticorrelations in resting state networks without global signal regression. *NeuroImage*, *59*(2), 1420–1428. https://doi.org/10.1016/j.neuroimage.2011.08.048

Chen, G., Chen, G., Xie, C., & Li, S.-J. (2011). Negative Functional Connectivity and Its Dependence on the Shortest Path Length of Positive Network in the Resting-State Human Brain. *Brain Connectivity*, *1*(3), 195–206. https://doi.org/10.1089/brain.2011.0025

Chéreau, R., Saraceno, G. E., Angibaud, J., Cattaert, D., & Nägerl, U. V. (2017). Superresolution imaging reveals activity-dependent plasticity of axon morphology linked to changes in action potential conduction velocity. *Proceedings of the National Academy of Sciences*, *114*(6), 1401–1406. https://doi.org/10.1073/pnas.1607541114

Christiansen, C. F. (2012). Risk of vascular disease in patients with multiple sclerosis: A review. *Neurological Research*, *34*(8), 746–753. https://doi.org/10.1179/1743132812Y.0000000051

Darquié, A., Poline, J.-B., Poupon, C., Saint-Jalmes, H., & Le Bihan, D. (2001). Transient decrease in water diffusion observed in human occipital cortex during visual stimulation. *Proceedings of the National Academy of Sciences*, *98*(16), 9391–9395. https://doi.org/10.1073/pnas.151125698

Diao, Y., Yin, T., Gruetter, R., & Jelescu, I. O. (2021). PIRACY: An Optimized Pipeline for Functional Connectivity Analysis in the Rat Brain. *Frontiers in Neuroscience*, *15*. Retrieved October 18, 2023, from https://www.frontiersin.org/articles/10.3389/fnins.2021.602170

Ding, Z., Huang, Y., Bailey, S. K., Gao, Y., Cutting, L. E., Rogers, B. P., Newton, A. T., & Gore, J. C. (2018). Detection of synchronous brain activity in white matter tracts at rest and under functional loading. *Proceedings of the National Academy of Sciences of the United States of America*, *115*(3), 595–600. https://doi.org/10.1073/pnas.1711567115

Farahani, F. V., Karwowski, W., & Lighthall, N. R. (2019). Application of Graph Theory for Identifying Connectivity Patterns in Human Brain Networks: A Systematic Review. *Frontiers in Neuroscience*, *13*. Retrieved February 8, 2024, from https://www.frontiersin.org/journals/neuroscience/articles/10.3389/fnins.2019.00585

Finn, E. S., Shen, X., Scheinost, D., Rosenberg, M. D., Huang, J., Chun, M. M., Papademetris, X., & Constable, R. T. (2015). Functional connectome fingerprinting: Identifying individuals using patterns of brain connectivity. *Nature Neuroscience*, *18*(11), 1664–1671. https://doi.org/10.1038/nn.4135

Fox, M. D., Snyder, A. Z., Vincent, J. L., Corbetta, M., Van Essen, D. C., & Raichle, M. E. (2005). The human brain is intrinsically organized into dynamic, anticorrelated functional networks. *Proceedings of the National Academy of Sciences*, *102*(27), 9673–9678. https://doi.org/10.1073/pnas.0504136102

Fox, M. D., Zhang, D., Snyder, A. Z., & Raichle, M. E. (2009). The Global Signal and Observed Anticorrelated Resting State Brain Networks. *Journal of Neurophysiology*, *101*(6), 3270–3283. https://doi.org/10.1152/jn.90777.2008

Gati, J. S., Menon, R. S., Uğurbil, K., & Rutt, B. K. (1997). Experimental determination of the BOLD field strength dependence in vessels and tissue. *Magnetic Resonance in Medicine*, *38*(2), 296–302. https://doi.org/10.1002/mrm.1910380220

Gore, J. C., Li, M., Gao, Y., Wu, T.-L., Schilling, K. G., Huang, Y., Mishra, A., Newton, A. T., Rogers, B. P., Chen, L. M., Anderson, A. W., & Ding, Z. (2019). Functional MRI and resting state connectivity in white matter - a mini-review. *Magnetic Resonance Imaging*, *63*, 1–11. https://doi.org/10.1016/j.mri.2019.07.017

Grajauskas, L. A., Frizzell, T., Song, X., & D'Arcy, R. C. N. (2019). White Matter fMRI Activation Cannot Be Treated as a Nuisance Regressor: Overcoming a Historical Blind Spot. *Frontiers in Neuroscience*, *13*. Retrieved February 15, 2024, from https://www.frontiersin.org/journals/neuroscience/articles/10.3389/fnins.2019.01024

Griffanti, L., Douaud, G., Bijsterbosch, J., Evangelisti, S., Alfaro-Almagro, F., Glasser, M. F., Duff, E. P., Fitzgibbon, S., Westphal, R., Carone, D., Beckmann, C. F., & Smith, S. M. (2017). Hand classification of fMRI ICA noise components. *Neuroimage*, *154*, 188–205. https://doi.org/10.1016/j.neuroimage.2016.12.036

Griswold, M. A., Jakob, P. M., Heidemann, R. M., Nittka, M., Jellus, V., Wang, J., Kiefer, B., & Haase, A. (2002). Generalized autocalibrating partially parallel acquisitions (GRAPPA). *Magnetic Resonance in Medicine*, *47*(6), 1202–1210. https://doi.org/10.1002/mrm.10171

Jelescu, I. O., Ciobanu, L., Geffroy, F., Marquet, P., & Le Bihan, D. (2014). Effects of hypotonic stress and ouabain on the apparent diffusion coefficient of water at cellular and tissue levels in Aplysia. *NMR in Biomedicine*, *27*(3), 280–290. https://doi.org/10.1002/nbm.3061

Jin, T., & Kim, S.-G. (2008). Functional changes of apparent diffusion coefficient during visual stimulation investigated by diffusion-weighted gradient-echo fMRI. *NeuroImage*, *41*(3), 801–812. https://doi.org/10.1016/j.neuroimage.2008.03.014

Jin, T., Zhao, F., & Kim, S.-G. (2006). Sources of functional apparent diffusion coefficient changes investigated by diffusion-weighted spin-echo fMRI. *Magnetic Resonance in Medicine*, *56*(6), 1283–1292. https://doi.org/10.1002/mrm.21074

Jung, B. A., & Weigel, M. (2013). Spin echo magnetic resonance imaging. *Journal of Magnetic Resonance Imaging*, *37*(4), 805–817. https://doi.org/10.1002/jmri.24068

Karababa, I. F., Bayazıt, H., Kılıçaslan, N., Celik, M., Cece, H., Karakas, E., & Selek, S. (2015). Microstructural Changes of Anterior Corona Radiata in Bipolar Depression. *Psychiatry Investigation*, *12*(3), 367–371. https://doi.org/10.4306/pi.2015.12.3.367

Kellner, E., Dhital, B., Kiselev, V. G., & Reisert, M. (2016). Gibbs-ringing artifact removal based on local subvoxel-shifts. *Magnetic Resonance in Medicine*, *76*(5), 1574–1581. https://doi.org/10.1002/mrm.26054

Komaki, Y., Debacker, C., Djemai, B., Ciobanu, L., Tsurugizawa, T., & Bihan, D. L. (2020). Differential effects of aquaporin-4 channel inhibition on BOLD fMRI and diffusion fMRI responses in mouse visual cortex. *PLoS ONE*, *15*(5), e0228759. https://doi.org/10.1371/journal.pone.0228759

Kwon, J., Lee, S., Jo, Y., & Choi, M. (2023). All-optical observation on activity-dependent nanoscale dynamics of myelinated axons. *Neurophotonics*, *10*(1), 015003. https://doi.org/10.1117/1.NPh.10.1.015003

Le Bihan, D. (2019). What can we see with IVIM MRI? *NeuroImage*, *187*, 56–67. https://doi.org/10.1016/j.neuroimage.2017.12.062

Le Bihan, D., Urayama, S.-i., Aso, T., Hanakawa, T., & Fukuyama, H. (2006). Direct and fast detection of neuronal activation in the human brain with diffusion MRI. *Proceedings of the National Academy of Sciences of the United States of America*, *103*(21), 8263–8268. https://doi.org/10.1073/pnas.0600644103

Li, J., Biswal, B. B., Wang, P., Duan, X., Cui, Q., Chen, H., & Liao, W. (2019). Exploring the functional connectome in white matter. *Human Brain Mapping*, *40*(15), 4331–4344. https://doi.org/10.1002/hbm.24705

Li, J., Kong, R., Liégeois, R., Orban, C., Tan, Y., Sun, N., Holmes, A. J., Sabuncu, M. R., Ge, T., & Yeo, B. T. T. (2019). Global signal regression strengthens association between resting-state functional connectivity and behavior. *NeuroImage*, *196*, 126–141. https://doi.org/10.1016/j.neuroimage.2019.04.016

Li, M., Newton, A. T., Anderson, A. W., Ding, Z., & Gore, J. C. (2019). Characterization of the hemodynamic response function in white matter tracts for event-related fMRI. *Nature Communications*, *10*(1), 1140. https://doi.org/10.1038/s41467-019-09076-2

Ling, T., Boyle, K. C., Zuckerman, V., Flores, T., Ramakrishnan, C., Deisseroth, K., & Palanker, D. (2020). High-speed interferometric imaging reveals dynamics of neuronal deformation during the action potential. *Proceedings of the National Academy of Sciences*, *117*(19), 10278–10285. https://doi.org/10.1073/pnas.1920039117

Lund, T. E., Madsen, K. H., Sidaros, K., Luo, W.-L., & Nichols, T. E. (2006). Non-white noise in fMRI: Does modelling have an impact? *NeuroImage*, *29*(1), 54–66. https://doi.org/10.1016/j.neuroimage.2005.07.005

Lv, H., Wang, Z., Tong, E., Williams, L., Zaharchuk, G., Zeineh, M., Goldstein-Piekarski, A., Ball, T., Liao, C., & Wintermark, M. (2018). Resting-State Functional MRI: Everything That Nonexperts Have Always Wanted to Know. *AJNR: American Journal of Neuroradiology*, *39*(8), 1390–1399. https://doi.org/10.3174/ajnr.A5527

Mark, C. I., Mazerolle, E. L., & Chen, J. J. (2015). Metabolic and vascular origins of the BOLD effect: Implications for imaging pathology and resting-state brain function. *Journal of Magnetic Resonance Imaging*, *42*(2), 231–246. https://doi.org/10.1002/jmri.24786

Miller, K. L., Bulte, D. P., Devlin, H., Robson, M. D., Wise, R. G., Woolrich, M. W., Jezzard, P., & Behrens, T. E. J. (2007). Evidence for a vascular contribution to diffusion FMRI at high b value. *Proceedings of the National Academy of Sciences*, *104*(52), 20967–20972. https://doi.org/10.1073/pnas.0707257105

Murphy, K., Birn, R. M., Handwerker, D. A., Jones, T. B., & Bandettini, P. A. (2009). The impact of global signal regression on resting state correlations: Are anti-correlated networks introduced? *NeuroImage*, *44*(3), 893–905. https://doi.org/10.1016/j.neuroimage.2008.09.036

Murphy, K., & Fox, M. D. (2017). Towards a consensus regarding global signal regression for resting state functional connectivity MRI. *NeuroImage*, *154*, 169–173. https://doi.org/10.1016/j.neuroimage.2016.11.052

Norris, D. G. (2012). Spin-echo fMRI: The poor relation? *NeuroImage*, *62*(2), 1109–1115. https://doi.org/10.1016/j.neuroimage.2012.01.003

Nunes, D., Gil, R., & Shemesh, N. (2021). A rapid-onset diffusion functional MRI signal reflects neuromorphological coupling dynamics. *NeuroImage*, *231*, 117862. https://doi.org/10.1016/j.neuroimage.2021.117862

Olszowy, W., Diao, Y., & Jelescu, I. O. (2021, May). *Beyond BOLD: Evidence for diffusion fMRI contrast in the human brain distinct from neurovascular response* (preprint). Neuroscience. https://doi.org/10.1101/2021.05.16.444253

Pak, R. W., Hadjiabadi, D. H., Senarathna, J., Agarwal, S., Thakor, N. V., Pillai, J. J., & Pathak, A. P. (2017). Implications of neurovascular uncoupling in functional magnetic resonance imaging (fMRI) of brain tumors. *Journal of Cerebral Blood Flow and Metabolism: Official Journal of the International Society of Cerebral Blood Flow and Metabolism*, *37*(11), 3475–3487. https://doi.org/10.1177/0271678X17707398

Pampel, A., Jochimsen, T. H., & Möller, H. E. (2010). BOLD background gradient contributions in diffusion-weighted fMRI–comparison of spin-echo and twice-refocused spin-echo sequences. *NMR in biomedicine*, *23*(6), 610–618. https://doi.org/10.1002/nbm.1502

Penny, W. D., Friston, K. J., Ashburner, J. T., Kiebel, S. J., & Nichols, T. E. (2011, April). *Statistical Parametric Mapping: The Analysis of Functional Brain Images*. Elsevier.

Raichle, M. E., MacLeod, A. M., Snyder, A. Z., Powers, W. J., Gusnard, D. A., & Shulman, G. L. (2001). A default mode of brain function. *Proceedings of the National Academy of Sciences*, *98*(2), 676–682. https://doi.org/10.1073/pnas.98.2.676

Rubinov, M., & Sporns, O. (2010). Complex network measures of brain connectivity: Uses and interpretations. *NeuroImage*, *52*(3), 1059–1069. https://doi.org/10.1016/j.neuroimage.2009.10.003

Schölvinck, M. L., Maier, A., Ye, F. Q., Duyn, J. H., & Leopold, D. A. (2010). Neural basis of global resting-state fMRI activity. *Proceedings of the National Academy of Sciences*, *107*(22), 10238–10243. https://doi.org/10.1073/pnas.0913110107

Setsompop, K., Cohen-Adad, J., Gagoski, B. A., Raij, T., Yendiki, A., Keil, B., Wedeen, V. J., & Wald, L. L. (2012). Improving diffusion MRI using simultaneous multi-slice echo planar imaging. *NeuroImage*, *63*(1), 569–580. https://doi.org/10.1016/j.neuroimage.2012.06.033

Setsompop, K., Fan, Q., Stockmann, J., Bilgic, B., Huang, S., Cauley, S. F., Nummenmaa, A., Wang, F., Rathi, Y., Witzel, T., & Wald, L. L. (2018). High-resolution in vivo diffusion imaging of the human brain with Generalized SLIce Dithered Enhanced Resolution Simultaneous MultiSlice (gSlider-SMS). *Magnetic resonance in medicine*, *79*(1), 141. https://doi.org/10.1002/mrm.26653

Setsompop, K., Gagoski, B. A., Polimeni, J. R., Witzel, T., Wedeen, V. J., & Wald, L. L. (2012). Blipped-controlled aliasing in parallel imaging for simultaneous multislice echo planar imaging with reduced g-factor penalty. *Magnetic Resonance in Medicine*, *67*(5), 1210–1224. https://doi.org/10.1002/mrm.23097

Sherpa, A. D., Xiao, F., Joseph, N., Aoki, C., & Hrabetova, S. (2016). Activation of -adrenergic receptors in rat visual cortex expands astrocytic processes and reduces extracellular space volume. *Synapse (New York, N.Y.)*, *70*(8), 307–316. https://doi.org/10.1002/syn.21908

Soares, J. M., Magalhães, R., Moreira, P. S., Sousa, A., Ganz, E., Sampaio, A., Alves, V., Marques, P., & Sousa, N. (2016). A Hitchhiker's Guide to Functional Magnetic Resonance Imaging. *Frontiers in Neuroscience*, *10*. Retrieved November 16, 2023, from https://www.frontiersin.org/articles/10.3389/fnins.2016.00515

Spees, W. M., Lin, T.-H., & Song, S.-K. (2013). White-matter diffusion fMRI of mouse optic nerve. *NeuroImage*, *65*, 209–215. https://doi.org/10.1016/j.neuroimage.2012.10.021

Spencer, A., de Riedmatten, I., Nguyen-Duc, J., Szczepankiewicz, F., & Jelescu, I. (2024). Diffusion functional mri with isotropic b-tensor encoding. *Proc. Intl. Soc. Mag. Reson. Med.*, *3313*.

Sporns, O., Chialvo, D. R., Kaiser, M., & Hilgetag, C. C. (2004). Organization, development and function of complex brain networks. *Trends in Cognitive Sciences*, *8*(9), 418–425. https://doi.org/10.1016/j.tics.2004.07.008

Stampacchia, S., Asadi, S., Tomczyk, S., Ribaldi, F., Scheffler, M., Lövblad, K.-O., Pievani, M., Frisoni, G. B., Garibotto, V., & Amico, E. (2022, February). Fingerprinting of brain disease: Connectome identifiability in cognitive decline and neurodegeneration. https://doi.org/10.1101/2022.02.04.479112

Tjandra, T., Brooks, J. C. W., Figueiredo, P., Wise, R., Matthews, P. M., & Tracey, I. (2005). Quantitative assessment of the reproducibility of functional activation measured with BOLD and MR perfusion imaging: Implications for clinical trial design. *NeuroImage*, *27*(2), 393–401. https://doi.org/10.1016/j.neuroimage.2005.04.021

Tsurugizawa, T., Ciobanu, L., & Le Bihan, D. (2013). Water diffusion in brain cortex closely tracks underlying neuronal activity. *Proceedings of the National Academy of Sciences*, *110*(28), 11636–11641. https://doi.org/10.1073/pnas.1303178110

Uğurbil, K., Xu, J., Auerbach, E. J., Moeller, S., Vu, A. T., Duarte-Carvajalino, J. M., Lenglet, C., Wu, X., Schmitter, S., Van de Moortele, P. F., Strupp, J., Sapiro, G., De Martino, F., Wang, D., Harel, N., Garwood, M., Chen, L., Feinberg, D. A., Smith, S. M., . . . WU-Minn HCP Consortium. (2013). Pushing spatial and temporal resolution for functional and diffusion MRI in the Human Connectome Project. *NeuroImage*, *80*, 80–104. https://doi.org/10.1016/j.neuroimage.2013.05.012

van den Heuvel, M. P., & Hulshoff Pol, H. E. (2010). Exploring the brain network: A review on resting-state fMRI functional connectivity. *European Neuropsychopharmacology*, *20*(8), 519–534. https://doi.org/10.1016/j.euroneuro.2010.03.008

Veraart, J., Novikov, D. S., Christiaens, D., Ades-aron, B., Sijbers, J., & Fieremans, E. (2016). Denoising of diffusion MRI using random matrix theory. *NeuroImage*, *142*, 394–406. https://doi.org/10.1016/j.neuroimage.2016.08.016

Wakana, S., Jiang, H., Nagae-Poetscher, L. M., van Zijl, P. C. M., & Mori, S. (2004). Fiber Tract–based Atlas of Human White Matter Anatomy. *Radiology*, *230*(1), 77–87. https://doi.org/10.1148/radiol.2301021640

Watts, D. J., & Strogatz, S. H. (1998). Collective dynamics of 'small-world' networks. *Nature*, *393*(6684), 440–442. https://doi.org/10.1038/30918

Weissenbacher, A., Kasess, C., Gerstl, F., Lanzenberger, R., Moser, E., & Windischberger, C. (2009). Correlations and anticorrelations in resting-state functional connectivity MRI: A quantitative comparison of preprocessing strategies. *NeuroImage*, *47*(4), 1408–1416. https://doi.org/10.1016/j.neuroimage.2009.05.005

West, K. L., Zuppichini, M. D., Turner, M. P., Sivakolundu, D. K., Zhao, Y., Abdelkarim, D., Spence, J. S., & Rypma, B. (2019). BOLD hemodynamic response function changes significantly with healthy aging. *NeuroImage*, *188*, 198–207. https://doi.org/10.1016/j.neuroimage.2018.12.012

Xu, X., Yuan, H., & Lei, X. (2016). Activation and Connectivity within the Default Mode Network Contribute Independently to Future-Oriented Thought. *Scientific Reports*, *6*(1), 21001. https://doi.org/10.1038/srep21001

Zhang, D., Johnston, J. M., Fox, M. D., Leuthardt, E. C., Grubb, R. L., Chicoine, M. R., Smyth, M. D., Snyder, A. Z., Raichle, M. E., & Shimony, J. S. (2009). Preoperative sensorimotor mapping in brain tumor patients using spontaneous fluctuations in neuronal activity imaged with functional magnetic resonance imaging: Initial experience. *Neurosurgery*, *65*(6 Suppl), 226–236. https://doi.org/10.1227/01.NEU.0000350868.95634.CA

Zuo, X.-N., Di Martino, A., Kelly, C., Shehzad, Z. E., Gee, D. G., Klein, D. F., Castellanos, F. X., Biswal, B. B., & Milham, M. P. (2010). The oscillating brain: Complex and reliable. *NeuroImage*, *49*(2), 1432–1445. https://doi.org/10.1016/j.neuroimage.2009.09.037